Developmental Biology 516 (2024) 122–129

Contents lists available at ScienceDirect

Developmental Biology

journal homepage: www.elsevier.com/locate/developmentalbiology

Registered Report Stage II

Visualizing metabolic regulation using metabolic biosensors during sea urchin embryogenesis

Aidan Furze [1], Ashley Waldron [1], Mamiko Yajima [*]

Department of Molecular Biology Cell Biology Biochemistry, Brown University, 185 Meeting Street, BOX-GL277, Providence, RI, 02912, USA

ARTICLE INFO

Keywords:
Metabolic regulation
Pyruvate sensor
Embryonic development
Sea urchin

ABSTRACT

Growing evidence suggests that metabolic regulation directly influences cellular function and development and thus may be more dynamic than previously expected. In vivo and in real-time analysis of metabolite activities during development is crucial to test this idea directly. In this study, we employ two metabolic biosensors to track the dynamics of pyruvate and oxidative phosphorylation (Oxphos) during the early embryogenesis of the sea urchin. A pyruvate sensor, PyronicSF, shows the signal enrichment on the mitotic apparatus, which is consistent with the localization patterns of the corresponding enzyme, pyruvate kinase (PKM). The addition of pyruvate increases the PyronicSF signal, while PKM knockdown decreases its signal, responding to the pyruvate level in the cell. Similarly, a ratio-metric sensor, Grx-roGFP, that reads the redox potential of the cell responds to DTT and H_2O_2, the known reducer and inducer of Oxphos. These observations suggest that these metabolic biosensors faithfully reflect the metabolic status in the cell during embryogenesis. The time-lapse imaging of these biosensors suggests that pyruvate and Oxphos levels change both spatially and temporarily during embryonic development. Pyruvate level is increased first in micromeres compared to other blastomeres at the 16-cell stage and remains high in ectoderm while decreasing in endomesoderm during gastrulation. In contrast, the Oxphos signal first decreases in micromeres at the 16-cell stage, while it increases in the endomesoderm during gastrulation, showing the opposite trend of the pyruvate signal. These results suggest that metabolic regulation is indeed both temporally and spatially dynamic during embryogenesis, and these biosensors are a valuable tool to monitor metabolic activities in real-time in developing embryos.

1. Introduction

Metabolic regulation is critical for general energy maintenance in the cell. However, recent reports suggest that glycolysis and other metabolic regulations may be necessary for specific cell signaling and differentiation in certain cell types (Peng et al., 2016; Yuan et al., 2020; Machler et al., 2016). For example, in cancer cells, aerobic glycolysis (Warburg effect) has been proposed to be essential for cell proliferation for a long time (Vander Heiden et al., 2009). However, recent studies suggest that aerobic glycolysis may be critical to the presomitic mesoderm patterning (Bulusu et al., 2017; Oginuma et al., 2017, 2020) or trophectoderm differentiation (Chi et al., 2020) rather than cell proliferation during vertebrate embryonic patterning. Further, progressive upregulation or transition from glycolysis to oxidative phosphorylation (Oxphos) is reported to be critical for neural and immune cell differentiation (Zheng et al., 2016; Price et al., 2018). These observations suggest that metabolic activity is dynamic. Especially, a balance between glycolysis and Oxphos may play critical roles in cell differentiation during development other than providing the energy for cellular maintenance.

To test this hypothesis directly, it is critical to analyze glycolytic and Oxphos regulation *in vivo* and *in real-time* in developing organisms. In this study, we employ two recently developed metabolic biosensors to test if specific metabolic regulations are spatially and temporally dynamic during the embryogenesis of the sea urchin. The sea urchin embryo is selected as a quick model system here since it completes the initial embryonic patterning, such as gastrulation, within 48 h post fertilization (48 hpf). Further, cells are transparent and suitable for time-lapse imaging of the developmental processes throughout embryogenesis, allowing us to track the molecular dynamics *in real-time*.

The biosensors tested in this study include PyronicSF, a pyruvate sensor, and Grx1-roGFP, a redox potential sensor that reflects oxidative phosphorylation (OxPhos). Pyruvate is a metabolite synthesized at the

* Corresponding author. MCB Department, Brown University, 185 Meeting Street, BOX-GL277, Providence, RI, 02912, USA.
E-mail address: Mamiko_Yajima@brown.edu (M. Yajima).
[1] These authors contributed equally.

https://doi.org/10.1016/j.ydbio.2024.08.003
Received 13 June 2024; Received in revised form 1 August 2024; Accepted 2 August 2024
Available online 6 August 2024

last step of glycolysis and is a part of carbohydrate metabolism. It is processed by pyruvate kinase (PKM). PyronicSF, a GFP-based sensor, houses the sequence of bacterial transcription factor PdhR linked to a circularly-permuted version of GFP (cpGFP) (Arce-Molina et al., 2020). This is a revised sensor from the original FRET-based Pyronic sensor (San Martin et al., 2014). The fluorescence level of PyronicSF is reported to change dynamically based on the amount of pyruvate available in the cell, allowing real-time subcellular quantitation of pyruvate transport, concentration, and flux in mouse neuronal cells and brain tissue of *Drosophila* larvae (Arce-Molina et al., 2020).

Grx1-roGFP is a ratio-metric sensor that reflects the Oxphos level in the cell (Gutscher et al., 2008). It consists of human glutaredoxin-1 (Grx1) linked to a redox-sensitive GFP (roGFP). roGFP contains a redox-reactive dithiol-disulfide pair in the structure, which changes the fluorescent properties based on oxidation and is ratiometric by excitation (Hanson et al., 2004). This biosensor is reported to detect a change between the reduced glutathione and the oxidized glutathione in seconds to minutes, thus measuring the glutathione redox potential in real-time, reflecting the activity of the tricarboxylic acid (TCA) cycle and OxPhos in the cell (Gutscher et al., 2008; Meyer et al., 2007; Stapper and Jahn, 2018; Albrecht et al., 2014).

In this study, we demonstrate that both PyronicSF and Grx1-roGFP biosensors faithfully reflect the metabolic status in the cell and are sensitive enough to track the dynamics throughout the embryogenesis of the sea urchin with no apparent cytotoxicity. These biosensors will be helpful in broadening applications in the future to understand how metabolic regulation impacts developmental processes together with gene and protein regulations in various model systems.

2. Materials and methods

2.1. Animals and embryo culture

0.5 M KCl was injected into adult sea urchins to collect eggs and sperm. For fertilization of eggs, 1 mM 3-amino triazole (Sigma, St. Louis, MO, USA) was added to the seawater filtered with the 0.22 μm pore filter to prevent the cross-linking of fertilization envelopes. The fertilized eggs were cultured to be a single layer in the dish (approximately 0.5 mL packed eggs per 15 mL filtered seawater) at 16 °C until the desired developmental stage.

2.2. Construct generation and microinjection

Open Reading Frame (ORF) of each gene of interest was PCR-amplified from the Addgene plasmids for PyronicSF (#124812) and Grx1-roGFP (#64975; Gutscher et al., 2008), or the *Sp* cDNA library for *Sp-pkm2* (XM_031000415.1) gene. The amplified PCR product was then inserted in the pSP64 vector for in vitro transcription. All subcloning procedures were performed using the In-Fusion HD Cloning kit (Takara) following the manufacturer's protocol. Vasa-mCherry, 2xmCherry-EMTB, and membrane-mCherry were all previously constructed (Uchida and Yajima, 2018; Wavreil et al., 2021). For in vitro transcription (IVT), each construct was linearized overnight with SalI, SmaI, or NotI, purified, and processed for IVT using the mMESSAGE mMACHINE® SP6 Transcription Kit (Thermo Fisher; catalog #AM1340) by following the manufacturer's protocol. PyronicSF and Grx1-roGFP mRNAs were microinjected at 1.5 μg/μL and 500 ng/μL, respectively, along with membrane-mCherry at 200–300ng/μL into the fertilized eggs of the sea urchin. Morpholino antisense oligo for Sp-*PKM2* (PKM2-MO: AAGCCATGATGATCGGAGATGATGA) was injected with a final concentration of 0.1 mM. Please see Table S1 for further details. Embryos were injected with 6∼10 pL of injection mixture and cultured up to the desired developmental stage. The resulting embryos were cultured up to the desired developmental stage. All imaging was performed under the Nikon CSU-W1 Spinning disk microscope.

2.3. Chemical treatment

For treatment with pyruvate, embryos were transferred to the filtered seawater containing 10 mM pyruvate at the 16-cell stage or gastrula stage and imaged immediately in the solution with no pre-incubation time. For treatments with 10 μM DTT or 1 mM H2O2, gastrula-stage embryos were incubated in the relevant chemical for 30 min prior to confocal imaging, followed by 10 min of imaging in the chemical solution.

2.4. Image processing and statistical analyses for imaging

For all confocal images, pseudocolor images (and ratiometric pseudocolor images) were created using Nikon's NIS elements software. For PyronicSF injected embryos, region of interest (ROI) measurements were used to gather signal intensity of both the 488 (pseudocolor green, PyronicSF) and 561 (pseudocolor pink, membrane-mCherry or 2xmCherry-EMTB), and the data was normalized as follows and labeled as "relative intensity": Value of green emission from 488 excitation/Value of green emission from 561 excitation. For the Grx1-roGFP2 injected embryos, ROI measurements were used to gather the ratiometric value as follows and labeled as "relative intensity": Value of green emission from 405 excitation/Value of green emission from 488 excitation. For other image analysis, FIJI (NIH) or Nikon NIS-Elements were used. The statistical significance was determined by PRISM (GraphPad) using paired t-tests for experiments with two groups or one-way ANOVA with Tukey's multiple comparisons post-hoc tests. For one-way ANOVA analyses, multiple comparisons were conducted to compare all treatments to the control. P values less than 0.05 were considered significant. Asterisks were used to indicate significance corresponding with * is $p < 0.05$, ** is $p < 0.01$, *** is $p < 0.001$, **** is $p < 0.0001$. Columns represent means ± SD or SEM.

2.5. Immunofluorescence

Embryos were fixed with 90% ice-cold methanol, followed by washing with PBS three times. The fixed embryos were incubated with a rabbit polyclonal anti-PKM2 antibody (GeneTex, GTX107977) at 1:100 and mouse monoclonal anti-Tubulin antibody (Cell signaling, D3U1W) at 1:200 dilutions, followed by the corresponding secondary antibodies conjugated with Alexa 555 and Alexa 488, respectively. The resultant embryos were imaged on the Nikon CSU-W1 Spinning disk microscope, and the NIS Elements or *FIJI* (NIH) was used for imaging processing. Please see Table S1 for further details.

2.6. Immunoblot analysis

The proteins were collected from each embryo group at the desired stage in 20 μL of loading buffer. Each sample (2–10 μL) was then run on a 10% Tris-glycine polyacrylamide gel and transferred to nitrocellulose membranes for immunoblotting with PKM or Actin primary antibody at 1:1000 or 1:4000, respectively, followed by incubation with HRP-conjugated anti-mouse or -rabbit secondary antibodies at 1: 2000 (Cell Signaling Technologies), respectively. The bound antibodies were detected by incubation in a chemiluminescence solution (1.25 mM luminol, 68 μM coumaric acid, 0.0093% hydrogen peroxide, and 0.1 M Tris pH 8.6) and imaged on Chemidoc (Bio-Rad, USA) with 1∼5 min exposure. Experiments were performed at least two independent times. Please see Table S1 for further details.

3. Results

3.1. PKM and PyronicSF localize on the mitotic apparatus during early embryogenesis of the sea urchin

Before testing the pyruvate biosensor, we first analyzed the

expression dynamics of PKM since little information has been available about sea urchin pyruvate or its enzyme. The sea urchin, *Strongylocentrotus purpuratus*, appears to have a single *pkm*. PKM immunofluorescence and PKM-mCherry live reporter imaging of the 16-cell stage embryo showed that PKM protein is localized on the spindle as well as at the cortex of every blastomere. We found that the PKM signal is further enriched in micromeres that are formed through an asymmetric cell division at the 16-dell stage (Fig. 1A and B). The same PKM antibody also detected a major band at the 65 kDa with additional minor bands by immunoblot, which was all reduced by the morpholino antisense oligo that blocks the translation of PKM (PKM MO, Fig. 1C), suggesting the signal specificity of the PKM antibody in these embryos.

The pyruvate biosensor PyronicSF showed a signal enrichment on the mitotic apparatus and in the nucleus of micromeres at the 16-cell stage (Fig. 1D). This signal enrichment has spread to all blastomeres by the 28-32-cell stage (Fig. 1E). However, the nuclear signal in non-micromere blastomeres appeared much weaker compared to that in micromeres (Fig. 1E, arrowhead) or the signal on the mitotic apparatus (Fig. 1E, arrows). These observations suggest that PyronicSF has dynamic signal patterns during cell cycling.

To test the specificity of the PyronicSF signal, we added pyruvate to the culture media prior to imaging, which increased the relative PyronicSF levels ~1.5 times both at the 16-cell and gastrula (Day 2) stages as predicted (Fig. 2A) (Arce-Molina et al., 2020). In contrast, PKM-MO knockdown reduced the relative PyronicSF signal to half at the 16-cell stage (Fig. 2B). Further, it caused significant developmental defects by Day 2 (Fig. 2C). The addition of PKM-mRNA to these PKM-MO embryos rescued the PyronicSF signal at the Day 1 and Day 2 stages (Fig. 2D and E). However, the development at Day 2 was only partially rescued, likely due to the imbalance between PKM knockdown and overexpression.

Overall, these results suggest that PyronicSF responds faithfully in the presence or absence of pyruvate or PKM activities. Further, it appears that the amount of PKM in the cell needs tight control during embryogenesis. These observations align with the fact that PKM is a rate-limiting factor of glycolysis. For example, in cancer cells, the excess PKM activity could shift the cellular metabolism to the Warburg effect, facilitating tumor growth (Zuo et al., 2021). In contrast, its insufficient activity could reduce ATP synthesis, triggering mitochondrial biogenesis and autophagy in the cell (Prakasam et al., 2017). Further, PKM has multiple essential functions such as cell cycle regulation, transcriptional regulation, zygotic gene activation, and translational regulation of endoplasmic reticulum-destined mRNAs on top of its initially reported function in glycolysis (Jiang et al., 2014; Gao et al., 2012; Simsek et al., 2017; Nagaraj et al., 2017). Notably, many metabolic enzymes have multiple functions outside of their original roles in metabolic regulation (Ciesla, 2006; Jeffery, 2017). Therefore, using a metabolic biosensor that directly reflects the metabolite level is essential to determine the activity of PKM or other enzymes, specifically in metabolic regulation.

3.2. *Pyruvate shows dynamic distribution patterns during embryogenesis*

To test how pyruvate changes the dynamics during development, we time-lapse imaged the PyronicSF signal every 5 min from the 8-cell to unhatched blastula stages (Day 1). Membrane-mCherry was co-introduced to counterstain the cellular outlines. Under this imaging condition, the PyronicSF signal was bright enough to be detected

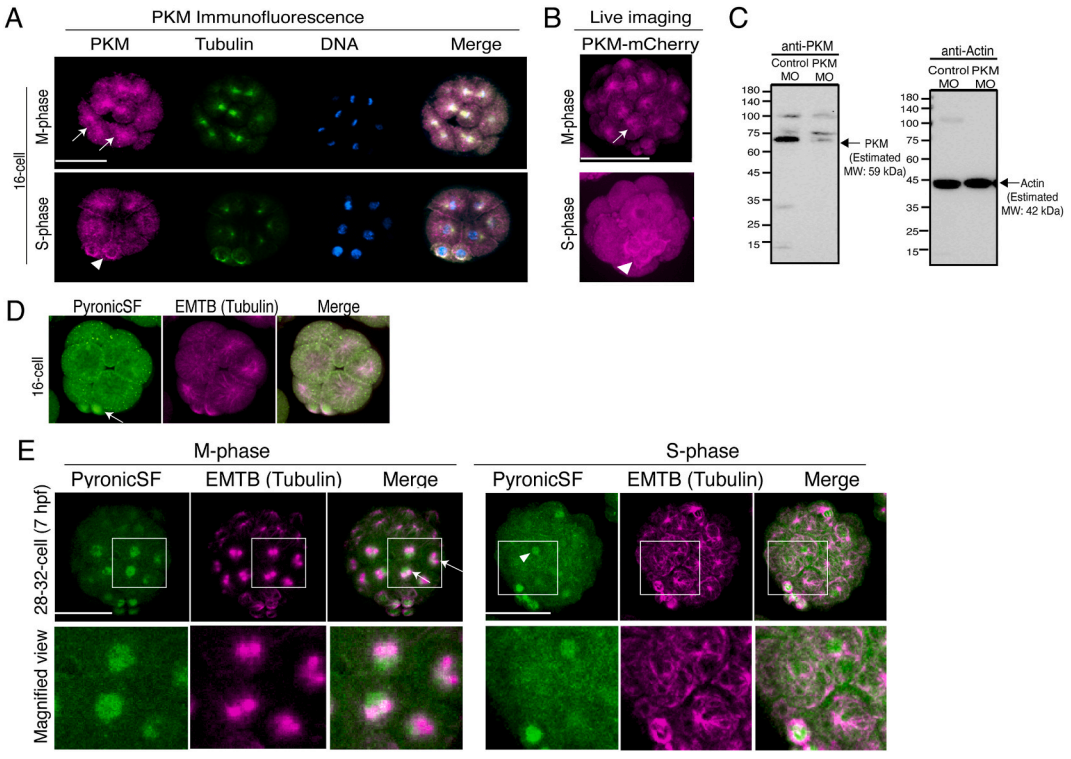

Fig. 1. PKM and PyronicSF localize on the mitotic apparatus in the early sea urchin embryo.
(A–B) Immunofluorescence of PKM (magenta) and tubulin (green) (A). PKM shows a similar signal pattern to PKM-mCherry (B). n = 30 or more, 90% of embryos showed the representative phenotypes shown in the images. (C) Proteins of the embryos injected with 1 mM Control-MO or PKM-MO were collected on Day 1 and detected by anti-PKM (left) or anti-Actin antibody (right). The PKM signal showed up in multiple bands, with a major band at 65 kDa in this study, which is slightly higher than the expected molecular weight of 59 kDa. In the PKM-MO group, all bands were reduced. The Actin signal (loading standard) stayed consistent in both groups. The multiple PKM bands may indicate the incomplete dissociation of PKM dimers for the higher bands due to the residual seawater in the embryo lysate and different isoforms of PKM or PKM proteins degraded during the immunoblot process for the lower bands. These experiments were conducted at least twice. (D–E) PyronicSF (green) shows its nuclear signal first in the micromers (D, arrow) and around the mitotic apparatus that is counter-stained by 2x mCherry-EMTB (microtubule marker; magenta) at the 28–32 cell stage (E, arrows). n = 30 or more, 90% of embryos showed the representative phenotypes presented in the images. All experiments were performed at least three independent times. All scale bars = 50 μm.

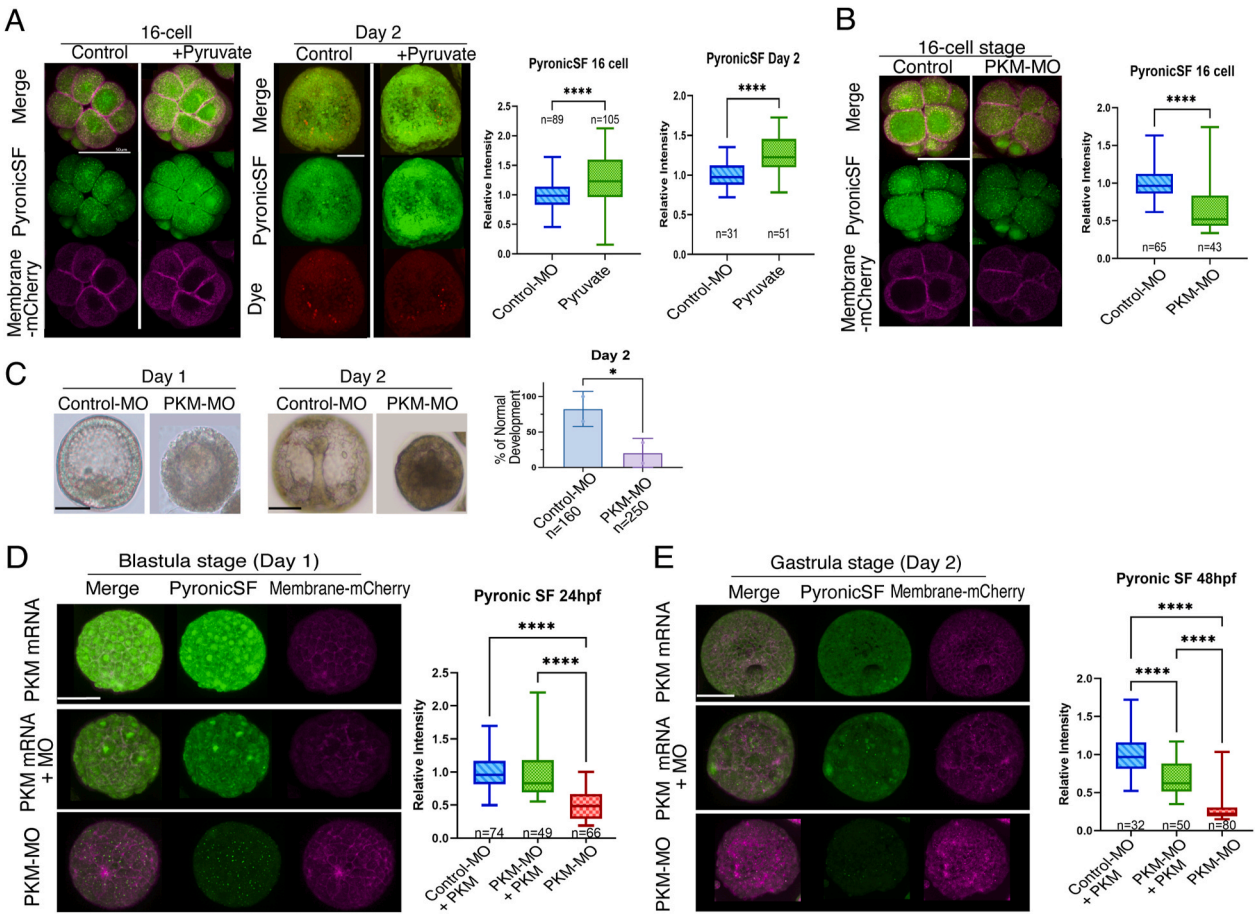

Fig. 2. Validation of PyronicSF metabolic sensor

Zygotes were microinjected with PyronicSF and membrane-mCherry as a counter-staining. The PyronicSF (green) signal intensities were measured, and each value was normalized to that of the mCherry (pink) or injection dye (red) signal to calculate the relative intensity level per embryo. All graphs in this figure indicate the relative intensity level of PyronicSF. (A) The embryos were treated with 10 mM pyruvate at the 16-cell stage or Day 2 and imaged immediately. (B–C) Zygotes were also co-introduced with 0.1 mM PKM-MO and imaged at the 16-cell stage for PyronicSF (B) and phenotyping (C). (D–E) Zygotes were injected with PKM-MO and PKM-mCherry for rescue and imaged at Day 1 (D) and Day 2 (E). n = indicates the total number of embryos analyzed for each group. All experiments were performed at least three independent times. All scale bars = 50 μm.

throughout early embryogenesis without showing any noticeable cytotoxicity. As seen in still images, the PyronicSF signal started in the micromeres at the 16-cell stage. It became uniformly enriched on the mitotic apparatus or in the nucleus throughout the embryo for the rest of the embryogenesis (Fig. 3A and B, arrows). The time-lapse imaging further clarifies the cell cycle-dependent dynamics of PyronicSF, which shows the signal increase during the M-phase on the mitotic apparatus compared to the signal level in the nucleus during the S-phase (Movie S1). Next, we time-lapse imaged every 35 min from the mesenchyme blastula to the gastrula stages (Days 1–2). The relative PyronicSF signal level was higher in the ectoderm and lower in the endomesoderm (Fig. 3C and D; Movie S2). Further, the germline marked by a germline factor Vasa (Voronina et al., 2008) showed a diminished PyronicSF signal (Fig. 3E). The nuclear signal of PyronicSF was most prominent before the blastula stage. It gradually disappeared over time by the gastrula stage (Day 2) (Fig. 3C).

Overall, these results suggest that pyruvate first enters the nucleus of the micromeres at the 16-cell stage and rapidly expands its nuclear localization to the entire embryo after this stage. After the blastula stage, however, the pyruvate decreases in the endomesoderm germ layer compared to the ectoderm layer. The metabolic asymmetry within an embryo appears to be prominent at key developmental time points for cellular differentiation, namely the 16-cell stage and at gastrulation.

3.3. *Oxidative phosphorylation is increased in the endomesoderm during gastrulation*

Next, we tested another biosensor, Grx1-roGFP, in the sea urchin embryo. We treated Day 2 gastrula embryos introduced with Grx1-roGFP with either 10 μM DTT or 1 mM H_2O_2 for 30 min prior to imaging. DTT and H_2O_2 are the known reducers and inducers of Oxphos (Gutscher et al., 2008). We measured the intensity value of the 509 nm (green) emission detected by a 405 nm laser excitation and then normalized that value by the green emission signal detected by a 488 nm laser excitation. Membrane-mCherry mRNA was also co-injected, yet it was only used as a general reference of mRNA translation in the embryo. The ratio of fluorescence intensity from excitation at 405/488 of Grx1-roGFP successfully increased and decreased, respectively, in the presence of 1 mM H_2O_2 and 10 μM DTT (Gutscher et al., 2008), suggesting that this ratiometric redox sensor also reflects the status of the Oxphos in the sea urchin embryo (Fig. 4A).

The timelapse imaging throughout embryogenesis suggests that this sensor shows a trend opposite to that of PyronicSF. Its signal was reduced in the micromere at the 16-cell stage (Fig. 4B, arrows; Movie S3) and increased in the future endomesoderm during gastrulation (Fig. 4C; Movie S4). Importantly, the primordial germ cells (PGCs) consistently showed the most decreased signal (Fig. 4D), which is consistent with the previous report that found the PGCs' decreased mitochondria activity in the sea urchin embryo (Oulhen et al., 2017). These results suggest that

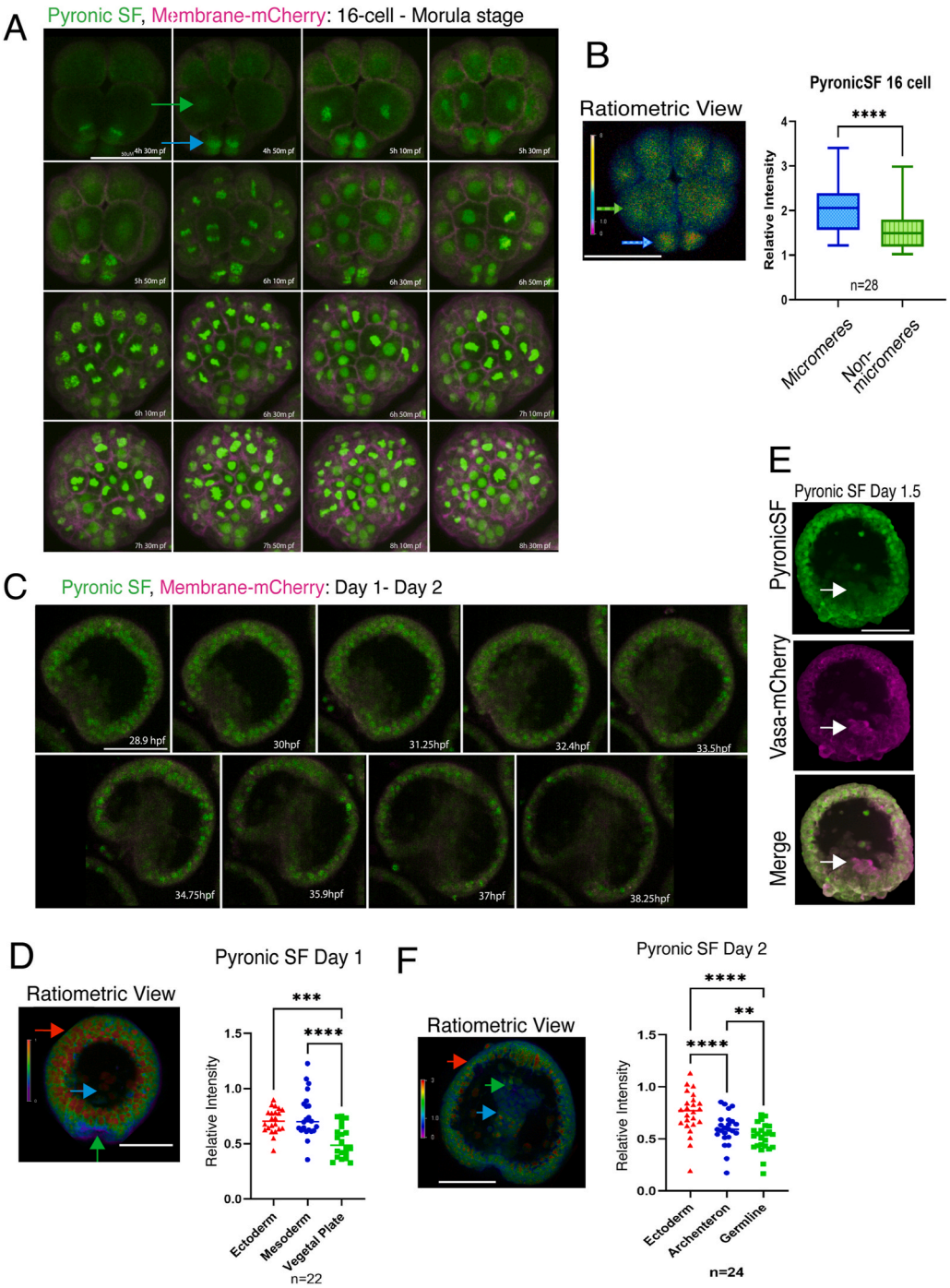

Fig. 3. Dynamic expression of PyronicSF during embryogenesis.
(A) The timelapse image series of PyronicSF (green), a pyruvate sensor, was counterstained with membrane-mCherry (magenta) from the 16-cell to morula stage. Images were taken every 5 min with a z-stack of 30 μm with 1 μm intervals. Only representative timepoints are shown. For complete panels, please see Movie S1. The time post-fertilization is indicated at the corner of each image. A blue arrow indicates a micromere and a green arrow indicates non-micromeres. (B) The heatmap images and the corresponding graph of the PyronicSF signal. The PyronicSF signal was normalized to the mCherry signal at the 16-cell(n = 28). The color scale for the heatmap ranging from red to blue indicates a higher or lower PyronicSF signal, respectively. The color of each arrow in the image indicates different cell lineages and corresponds to the color in the corresponding graph. (C) The timelapse image series of PyronicSF (green) counterstained with membrane-mCherry (magenta) from mesenchyme blastula to gastrula. Images were taken every 35 min with a z-stack of 30 μm with 1 μm intervals. Only representative images are shown. The time post-fertilization is indicated at the corner of each image. For complete panels, please see Movie S2. (D) The PyronicSF signal was normalized to the mCherry signal at blastula (n = 22) with the color scale for the heatmap ranging from red to blue, indicating higher or lower relative PyronicSF signals. The color of each arrow in the image indicates different cell lineages and corresponds to the color in each graph. (E) Expression patterns of PyronicSF (green) and germline marker Vasa-mCherry (magenta) during gastrulation (Day 1.5), with an arrow indicating the germline cells. (F). (F) The PyronicSF signal was normalized to the mCherry signal at gastrula (C, n = 25) with the color scale for the heatmap ranging from red to blue, indicating higher or lower relative PyronicSF signals. The color of each arrow in the image indicates different cell lineages and corresponds to the color in each graph. n = indicates the total number of embryos analyzed for each graph. All scale bars = 50 μm.

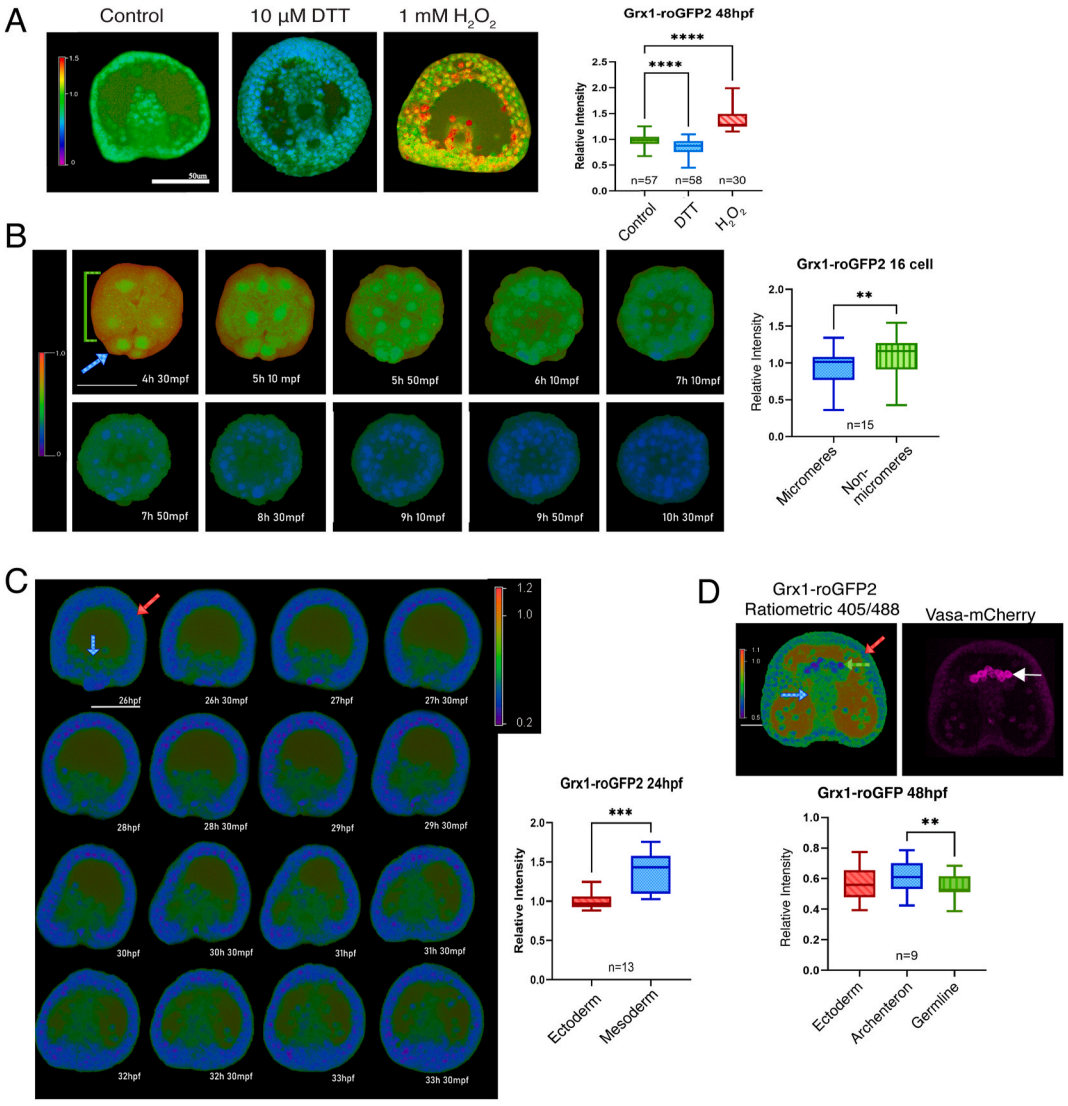

Fig. 4. Validation of Grx1-roGFP2 construct and time-lapse imaging of Grx1-roGFP2 biosensor during embryogenesis.
(A) Gastrula embryos introduced with Grx1-roGFP2 were treated with either 10 μM DTT or 1 mM H_2O_2 for 30 min prior to confocal imaging. The ratio signal of 405/488 is shown as a heatmap image. The relative value against the control group is shown in the graph. n = indicates the total number of embryos analyzed for each group. (B–C) Timelapse images of Grx1-roGFP either from the 16-cell stage to the blastula (B) or from the blastula to the gastrula (C). The signal ratio of 405/488 is shown as a heat map in each embryo image. (B) Images were taken every 40 min with a z-stack of ~30 μm with 1 μm intervals. Only representative images are shown. For total image panels, please see Movie S3. The hour post-fertilization is indicated at the corner of each image. A blue arrow indicates a micromere and a green bracket indicates non-micromeres, which corresponds to the color code in the graph (n = 9). (C) Images were taken every 15 min with a z-stack of ~30 μm with 1 μm intervals from the mesenchyme blastula to the gastrula stages. Only representative images are shown. For full image panels, please see Movie S4. The hour post-fertilization is indicated at the corner of each image. A blue arrow indicates the mesodermal lineage and a pink arrow indicates the ectodermal lineage, which corresponds to the color code in the corresponding graph (n = 13). (D) A ratiometric heatmap image of Grx1-roGFP in the gastrula embryo. A blue arrow indicates the endoderm, a pink arrow indicates the ectoderm and a green arrow indicates a germline that is counter-stained by Vasa (magenta), which corresponds to the color code in the graph. The signal ratio of 405/488 is shown as a heat map for each cell lineage. All experiments were performed at least three independent times. All scale bars = 50 μm.

oxidative phosphorylation is also asymmetric within an embryo at the 16-cell stage and during gastrulation, yet in the opposite dynamics to pyruvate.

4. Discussion

4.1. Metabolic activity is both temporally and spatially dynamic during embryogenesis of the sea urchin

In this study, we employed two metabolic sensors, which accurately responded to the metabolic changes in the cell. Throughout development, both pyruvate and Oxphos appear to undergo dynamic and asymmetric regulations at key developmental timepoints (Fig. 5). These timings include the 16-cell stage and gastrulation when the major cell lineage segregations occur, suggesting metabolic regulation is both temporally and spatially dynamic in accordance with developmental events. These results align with a recent report in the mouse embryo that used the isotopologue analysis to track downstream metabolites, which suggests the presence of metabolic reprogramming during early embryogenesis (Sharpley et al., 2021).

In this study, it is still unknown what causes the dynamic and asymmetric metabolic regulation during embryogenesis of the sea urchin. However, given that asymmetric metabolism is most evident at key developmental time points for differentiation, we speculate that one of

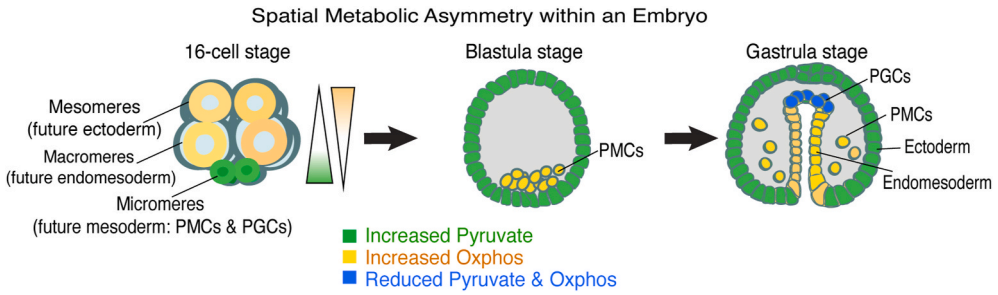

Fig. 5. A summary cartoon diagram depicting asymmetry and temporal dynamics of the metabolic sensors in the embryo. Pyruvate and oxidative phosphorylation sensors show dynamic yet antagonistic signal dynamics in each lineage except for the germline during the embryogenesis of the sea urchin.

two scenarios may be occurring: either the metabolic change facilitates the cell differentiation directly, as proposed in other models (Bulusu et al., 2017; Oginuma et al., 2017, 2020; Chi et al., 2020; Zheng et al., 2016; Price et al., 2018), or the different metabolic state is the consequence of cells differentiating into different cell fates with distinct properties. For the latter possibility, a recent study indicates that cells may use aerobic glycolysis when their demand for NAD+ is higher than their need for ATP to prioritize the specific downstream processes, such as amino acid and nucleotide synthesis (Luengo et al., 2021). Since newly differentiated cells might have different molecular and metabolic needs, they may favor different metabolic pathways for their specific downstream actions. However, these remaining questions need to be addressed through future studies.

In addition to the expected signal dynamics in response to the pyruvate or PKM knockdown, PyronicSF showed unique signal patterns on the spindle and nucleus in the sea urchin embryo. The spindle localization of PKM has been reported in several mammalian cell lines (Jiang et al., 2014; Gao et al., 2012). In these studies, PKM appears to regulate chromosome segregation or gene transcription by functioning as a kinase on the mitotic apparatus. Yet, its function in pyruvate synthesis has yet to be discovered in these studies. In the sea urchin embryo, we found that both PKM and pyruvate localize on the mitotic apparatus, casting a possibility of PKM functioning in pyruvate synthesis on the mitotic apparatus. It is vital to test in the future if/how the mitotic PKM and pyruvate contribute to metabolic regulation during early embryogenesis.

Further, the nuclear localization of pyruvate metabolism has also been reported in mammalian embryos (Nagaraj et al., 2017). Pyruvate Dehydrogenase, which converts pyruvate into acetyl-CoA, is transiently localized in the nucleus during early embryogenesis and facilitates zygotic gene activation in mouse and human embryos. In the sea urchin embryo, we found a similar transient nuclear localization of pyruvate. However, it showed more prolonged nuclear localization until the blastula stage and the gradual disappearance after Day 1. The sea urchin embryo divides every 30–40 min and is zygotically active from the 1-cell stage. The prolonged or gradual transition of nuclear pyruvate localization may indicate an extended or sequential zygotic activation to support the rapid development of the sea urchin embryo. However, further investigation is necessary to test whether nuclear pyruvate has a role in zygotic gene expression in the sea urchin embryo.

Lastly, a unique challenge of early embryo imaging with these sensors includes a maternal load of metabolites in the embryo, which could create a high background. In human cultured cells, PyronicSF is reported to change its signal level 2–3 times upon pyruvate addition, while we found that it was only ~1.5 times in the sea urchin embryo in this study. Further, the higher background with lipids and pigmentation in the embryo generally reduces the signal-to-noise ratio compared to the flat and transparent cultured cells in any fluorescence-based imaging. Nevertheless, these metabolic sensors are still powerful tools that output metabolic dynamics *in vivo* and *in real-time* without causing any noticeable cytotoxicity during a long period of imaging. In combination with gene perturbations and metabolic inhibitions in the future, these biosensors will be helpful in revealing how gene regulations and metabolic regulations are connected to govern complex embryogenesis.

Funding

This work was supported by the NIH (1R21HD109132-01) and NSF (IOS-1940975) to M.Y.

CRediT authorship contribution statement

Aidan Furze: Writing – review & editing, Visualization, Validation, Formal analysis, Data curation, Conceptualization. **Ashley Waldron:** Writing – review & editing, Writing – original draft, Visualization, Methodology, Formal analysis, Data curation, Conceptualization. **Mamiko Yajima:** Writing – review & editing, Writing – original draft, Visualization, Supervision, Resources, Project administration, Methodology, Investigation, Funding acquisition, Conceptualization.

Data availability

No data was used for the research described in the article.

Acknowledgments

A.F. and A.W. were responsible for conceptualization, experimental design, undertaking, data analysis, and manuscript construction. M.Y. was responsible for concepts, experimental design and undertaking, data analysis, manuscript construction, and editing.

Appendix A. Supplementary data

Supplementary data to this article can be found online at https://doi.org/10.1016/j.ydbio.2024.08.003.

References

Albrecht, S.C., Sobotta, M.C., Bausewein, D., Aller, I., Hell, R., Dick, T.P., Meyer, A.J., 2014. Redesign of genetically encoded biosensors for monitoring mitochondrial redox status in a broad range of model eukaryotes. J. Biomol. Screen 19 (3), 379–386. https://doi.org/10.1177/1087057113499634.

Arce-Molina, R., Cortes-Molina, F., Sandoval, P.Y., Galaz, A., Alegria, K., Schirmeier, S., Barros, L.F., San Martin, A., 2020. A highly responsive pyruvate sensor reveals pathway-regulatory role of the mitochondrial pyruvate carrier MPC. Elife 9. https://doi.org/10.7554/eLife.53917.

Bulusu, V., Prior, N., Snaebjornsson, M.T., Kuehne, A., Sonnen, K.F., Kress, J., Stein, F., Schultz, C., Sauer, U., Aulehla, A., 2017. Spatiotemporal analysis of a glycolytic activity gradient linked to mouse embryo mesoderm development. Dev. Cell 40 (4), 331–341 e334. https://doi.org/10.1016/j.devcel.2017.01.015.

Chi, F., Sharpley, M.S., Nagaraj, R., Roy, S.S., Banerjee, U., 2020. Glycolysis-independent glucose metabolism distinguishes TE from ICM fate during mammalian embryogenesis. Dev. Cell 53 (1), 9–26 e24. https://doi.org/10.1016/j.devcel.2020.02.015.

Ciesla, J., 2006. Metabolic enzymes that bind RNA: yet another level of cellular regulatory network? Acta Biochim. Pol. 53 (1), 11–32. https://www.ncbi.nlm.nih.gov/pubmed/16410835.

Gao, X., Wang, H., Yang, J.J., Liu, X., Liu, Z.R., 2012. Pyruvate kinase M2 regulates gene transcription by acting as a protein kinase. Mol. Cell 45 (5), 598–609. https://doi.org/10.1016/j.molcel.2012.01.001.

Gutscher, M., Pauleau, A.L., Marty, L., Brach, T., Wabnitz, G.H., Samstag, Y., Meyer, A.J., Dick, T.P., 2008. Real-time imaging of the intracellular glutathione redox potential. Nat. Methods 5 (6), 553–559. https://doi.org/10.1038/nmeth.1212.

Hanson, G.T., Aggeler, R., Oglesbee, D., Cannon, M., Capaldi, R.A., Tsien, R.Y., Remington, S.J., 2004. Investigating mitochondrial redox potential with redox-sensitive green fluorescent protein indicators. J. Biol. Chem. 279 (13), 13044–13053. https://doi.org/10.1074/jbc.M312846200.

Jeffery, C.J., 2017. Moonlighting proteins - nature's Swiss army knives. Sci. Prog. 100 (4), 363–373. https://doi.org/10.3184/003685017X15063357842574.

Jiang, Y., Li, X., Yang, W., Hawke, D.H., Zheng, Y., Xia, Y., Aldape, K., Wei, C., Guo, F., Chen, Y., Lu, Z., 2014. PKM2 regulates chromosome segregation and mitosis progression of tumor cells. Mol. Cell 53 (1), 75–87. https://doi.org/10.1016/j.molcel.2013.11.001.

Luengo, A., Li, Z., Gui, D.Y., Sullivan, L.B., Zagorulya, M., Do, B.T., Ferreira, R., Naamati, A., Ali, A., Lewis, C.A., Thomas, C.J., Spranger, S., Matheson, N.J., Vander Heiden, M.G., 2021. Increased demand for NAD(+) relative to ATP drives aerobic glycolysis. Mol. Cell 81 (4), 691–707 e696.

Machler, P., Wyss, M.T., Elsayed, M., Stobart, J., Gutierrez, R., von Faber-Castell, A., Kaelin, V., Zuend, M., San Martin, A., Romero-Gomez, I., Baeza-Lehnert, F., Lengacher, S., Schneider, B.L., Aebischer, P., Magistretti, P.J., Barros, L.F., Weber, B., 2016. In vivo evidence for a lactate gradient from astrocytes to neurons. Cell Metabol. 23 (1), 94–102. https://doi.org/10.1016/j.cmet.2015.10.010.

Meyer, A.J., Brach, T., Marty, L., Kreye, S., Rouhier, N., Jacquot, J.P., Hell, R., 2007. Redox-sensitive GFP in Arabidopsis thaliana is a quantitative biosensor for the redox potential of the cellular glutathione redox buffer. Plant J. 52 (5), 973–986. https://doi.org/10.1111/j.1365-313X.2007.03280.x.

Nagaraj, R., Sharpley, M.S., Chi, F., Braas, D., Zhou, Y., Kim, R., Clark, A.T., Banerjee, U., 2017. Nuclear localization of mitochondrial TCA cycle enzymes as a critical step in mammalian zygotic genome activation. Cell 168 (1–2), 210–223 e211. https://doi.org/10.1016/j.cell.2016.12.026.

Oginuma, M., Harima, Y., Tarazona, O.A., Diaz-Cuadros, M., Michaut, A., Ishitani, T., Xiong, F., Pourquie, O., 2020. Intracellular pH controls WNT downstream of glycolysis in amniote embryos. Nature 584 (7819), 98–101. https://doi.org/10.1038/s41586-020-2428-0.

Oginuma, M., Moncuquet, P., Xiong, F., Karoly, E., Chal, J., Guevorkian, K., Pourquie, O., 2017. A gradient of glycolytic activity coordinates FGF and wnt signaling during elongation of the body Axis in amniote embryos. Dev. Cell 40 (4), 342–353 e310. https://doi.org/10.1016/j.devcel.2017.02.001.

Oulhen, N., Swartz, S.Z., Laird, J., Mascaro, A., Wessel, G.M., 2017. Transient translational quiescence in primordial germ cells. Development 144 (7), 1201–1210. https://doi.org/10.1242/dev.144170.

Peng, M., Yin, N., Chhangawala, S., Xu, K., Leslie, C.S., Li, M.O., 2016. Aerobic glycolysis promotes T helper 1 cell differentiation through an epigenetic mechanism. Science 354 (6311), 481–484. https://doi.org/10.1126/science.aaf6284.

Prakasam, G., Singh, R.K., Iqbal, M.A., Saini, S.K., Tiku, A.B., Bamezai, R.N.K., 2017. Pyruvate kinase M knockdown-induced signaling via AMP-activated protein kinase promotes mitochondrial biogenesis, autophagy, and cancer cell survival. J. Biol. Chem. 292 (37), 15561–15576. https://doi.org/10.1074/jbc.M117.791343.

Price, M.J., Patterson, D.G., Scharer, C.D., Boss, J.M., 2018. Progressive upregulation of oxidative metabolism facilitates plasmablast differentiation to a T-independent antigen. Cell Rep. 23 (11), 3152–3159.

San Martin, A., Ceballo, S., Baeza-Lehnert, F., Lerchundi, R., Valdebenito, R., Contreras-Baeza, Y., Alegria, K., Barros, L.F., 2014. Imaging mitochondrial flux in single cells with a FRET sensor for pyruvate. PLoS One 9 (1), e85780. https://doi.org/10.1371/journal.pone.0085780.

Sharpley, M.S., Chi, F., Hoeve, J.T., Banerjee, U., 2021. Metabolic plasticity drives development during mammalian embryogenesis. Dev. Cell 56 (16), 2329–2347 e2326. https://doi.org/10.1016/j.devcel.2021.07.020.

Simsek, D., Tiu, G.C., Flynn, R.A., Byeon, G.W., Leppek, K., Xu, A.F., Chang, H.Y., Barna, M., 2017. The mammalian ribo-interactome reveals ribosome functional diversity and heterogeneity. Cell 169 (6), 1051–1065 e1018. https://doi.org/10.1016/j.cell.2017.05.022.

Stapper, Z.A., Jahn, T.R., 2018. Changes in glutathione redox potential are linked to abeta42-induced neurotoxicity. Cell Rep. 24 (7), 1696–1703. https://doi.org/10.1016/j.celrep.2018.07.052.

Uchida, A., Yajima, M., 2018. An optogenetic approach to control protein localization during embryogenesis of the sea urchin. Dev. Biol. 441 (1), 19–30. https://doi.org/10.1016/j.ydbio.2018.06.015.

Vander Heiden, M.G., Cantley, L.C., Thompson, C.B., 2009. Understanding the Warburg effect: the metabolic requirements of cell proliferation. Science 324 (5930), 1029–1033. https://doi.org/10.1126/science.1160809.

Voronina, E., Lopez, M., Juliano, C.E., Gustafson, E., Song, J.L., Extavour, C., George, S., Oliveri, P., McClay, D., Wessel, G., 2008. Vasa protein expression is restricted to the small micromeres of the sea urchin, but is inducible in other lineages early in development. Dev. Biol. 314 (2), 276–286. https://doi.org/10.1016/j.ydbio.2007.11.039.

Wavreil, F.D.M., Poon, J., Wessel, G.M., Yajima, M., 2021. Light-induced, spatiotemporal control of protein in the developing embryo of the sea urchin. Dev. Biol. 478, 13–24. https://doi.org/10.1016/j.ydbio.2021.06.006.

Yuan, Q., Miao, J., Yang, Q., Fang, L., Fang, Y., Ding, H., Zhou, Y., Jiang, L., Dai, C., Zen, K., Sun, Q., Yang, J., 2020. Role of pyruvate kinase M2-mediated metabolic reprogramming during podocyte differentiation. Cell Death Dis. 11 (5), 355. https://doi.org/10.1038/s41419-020-2481-5.

Zheng, X., Boyer, L., Jin, M., Mertens, J., Kim, Y., Ma, L., Ma, L., Hamm, M., Gage, F.H., Hunter, T., 2016. Metabolic reprogramming during neuronal differentiation from aerobic glycolysis to neuronal oxidative phosphorylation. Elife 5. https://doi.org/10.7554/eLife.13374.

Zuo, J., Tang, J., Lu, M., Zhou, Z., Li, Y., Tian, H., Liu, E., Gao, B., Liu, T., Shao, P., 2021. Glycolysis rate-limiting enzymes: Novel potential regulators of rheumatoid arthritis pathogenesis. Front. Immunol. 12, 779787 https://doi.org/10.3389/fimmu.2021.779787.